

Local Group galaxies emerge from the dark

Till Sawala^{1*}, Carlos S. Frenk¹, Azadeh Fattahi², Julio F. Navarro², Richard G. Bower¹, Robert A. Crain³, Claudio Dalla Vecchia^{4,5}, Michelle Furlong¹, John. C. Helly¹, Adrian Jenkins¹, Kyle A. Oman², Matthieu Schaller¹, Joop Schaye³, Tom Theuns^{1,6}, James Trayford¹ and Simon D. M. White⁷

¹Institute for Computational Cosmology, Department of Physics, University of Durham, South Road, Durham DH13LE, UK, ²Department of Physics and Astronomy, University of Victoria, 3800 Finnerty Road, Victoria, British Columbia V8P 5C2, Canada, ³Leiden Observatory, Leiden University, Postbus 9513, 2300 RA Leiden, The Netherlands, ⁴Instituto de Astrofísica de Canarias, C/ Vía Láctea s/n, 38205 La Laguna, Tenerife, Spain, ⁵Astrophysics Research Institute, Liverpool John Moores University, 146 Brownlow Hill, Liverpool L3 5RF, UK, ⁶Department of Physics, University of Antwerp, Campus Groenenborger, Groenenborgerlaan 171, B-2020 Antwerp, Belgium ⁷Max Planck Institute for Astrophysics, Karl-Schwarzschild-Str. 1, 85741 Garching, Germany

*To whom correspondence should be addressed; E-mail: till.sawala@durham.ac.uk

The “Lambda Cold Dark Matter” (Λ CDM) model of cosmic structure formation is eminently falsifiable: once its parameters are fixed on large scales, it becomes testable in the nearby Universe. Observations within our Local Group of galaxies, including the satellite populations of the Milky Way and Andromeda, appear to contradict Λ CDM predictions: there are far fewer satellite galaxies than dark matter halos (the “missing satellites” problem (1, 2)), galaxies seem to avoid the largest substructures (the “too big to fail” problem (3, 4)), and the brightest satellites appear to orbit their host galaxies on a thin plane (the “planes of satellites” problem (5)). We present results from the first hydrodynamic simulations of the Local Group that match the observed abundance of galaxies. We find that when baryonic and dark matter are followed simultaneously in the context of a realistic galaxy formation model, all three “problems” are resolved within the Λ CDM paradigm.

The ability of the cold dark matter model to predict observables on different scales and at different epochs lies at the root of its remarkable success. The anisotropy of the microwave background radiation and the large scale distribution of galaxies were predicted after the model was formulated, and have since been spectacularly validated by observations. However, observations on scales currently testable only within the Local Group (LG) have yielded results that no simulation to date has been able to reproduce. This has renewed interest in alternatives to Λ CDM, such as warm (6) or self-interacting (7) dark matter.

The problems reported as fatal for Λ CDM arise when observations are confronted with predictions from dark matter only (DMO) simulations that treat the cosmic matter content as a single collisionless fluid (3, 8), under the assumption that baryonic processes are unimportant. It has, of course, long been recognized that the distribution of light is not a precise tracer of dark matter, but simple models for populating dark matter structures with galaxies do not capture the complexity of galaxy formation physics, including the effect of baryons on the dark matter. On the other hand, full hydrodynamic simulations have previously either focussed on individual galaxies ignoring the LG environment, or have not yet been able to reproduce the LG dwarf galaxy population (9, 10).

Improvements in numerical techniques and in the modeling of astrophysical processes have recently lead to hydrodynamical simulations that are able to reproduce the observed galaxy population over large scales in cosmologically representative volumes, notably the ILLUSTRIS (11) and EAGLE (12) projects. Here, we test the small scale nature of the Λ CDM model with a new suite of cosmological hydrodynamical simulations starting from initial conditions tailored to match the LG environment, using the EAGLE hydrodynamics code. Applying state-of-the-art hydrodynamic simulation techniques to a realistic local environment allows us for the first time directly to confront Λ CDM predictions with observations in the critical, subgalactic regime.

In particular, we focus on pairs of halos that match the separation, approach velocity, and relative tangential velocity of the Milky Way (MW) and Andromeda (M31). From a large cosmological simulation, we have selected twelve pairs of halos with combined virial masses of $\sim 2.3 \pm 0.6 \times 10^{12} M_{\odot}$, in agreement with the most recent dynamical constraints (13, 14). Each region was resimulated at three different resolution levels (labelled “L3”, “L2” and “L1”), both as pure dark matter, and with the full hydrodynamic model. At our lowest, “L3”, resolution, the particle mass is comparable to the intermediate resolution EAGLE runs, while L2 and L1 improve on this by factors of 12 and 144, respectively. At the highest resolution, each of the main galaxies is simulated with more than 20 million particles, comparable to the highest resolution simulations of individual galaxies published to date. Further details can be found in the Supplementary Information.

Dark Matter substructures are abundant in our Local Group simulations, but due to the complexity of galaxy formation, starlight paints a very different picture. Fig. 1 shows the dark matter and starlight in one of our simulation volumes at redshift $z = 0$: galaxies appear as biased tracers of the dark matter, forming almost exclusively in the most massive halos. The top left panel shows the dark matter distribution on larger scales, revealing a cosmic filament that envelopes the two principal halos and most of the galaxies in the region. Also highlighted are the positions of the halos that host the eleven brightest satellites of one of the main halos. Analogous to the Milky Way satellite system, the alignment is indicative of a thin plane seen in projection, that is also aligned with the orientation of the filament.

The small insets in Fig. 1 show the stellar structure of some of the many galaxies formed in this simulation. The images use multi-band colors rendered using a spectrophotometric model. A variety of disk and spheroid morphologies, luminosities, colors, and sizes are clearly visible, reminiscent of the diversity of observed LG galaxies.

Fig. 2 shows the galaxy stellar mass functions in the simulations, both within 300 kpc from each of the two main galaxies (labelled “primary” and “secondary” in order of halo mass), as

well as within 2 Mpc from the LG barycenter. On average, primary and secondary galaxies have 20_{-6}^{+10} and 18_{-5}^{+8} satellites more massive than $M_* = 10^5 M_\odot$ inside 300 kpc, respectively, in good agreement with the observed number of MW and M31 satellites¹. Within 2 Mpc of the LG barycenter, there are ~ 60 galaxies presently known with $M_* > 10^5 M_\odot$ known: on average, our simulations produce 90_{-15}^{+20} . The modest number of luminous galaxies is in stark contrast to the very large number of dark matter halos found within the same volume, indicated by the grey shaded area in Fig. 2. While feedback from supernovae and stellar winds regulate star formation in those halos where a dwarf galaxy has formed, reionization has left most of the low mass halos completely dark (16).

That the simulations reproduce the stellar mass function of galaxies and satellites in the LG over all resolved mass scales is remarkable, given that these simulations use the very same parameters that match the shape and normalization of the galaxy stellar mass function in large cosmological volumes. Not only are our simulations free of the “missing satellites” problem, but the observed stellar mass functions of the LG environment and of the MW and M31 satellites are entirely consistent with Λ CDM.

We next consider the “too big to fail” problem (3): the observation that the brightest satellites of the Milky Way appear to shun the most massive dark halo substructures. A simple statement of the problem is given by the number of satellite halos with peak circular velocities (V_{\max}) above ~ 30 km/s. Only three MW satellites are consistent with halos more massive than this limit (the two Magellanic Clouds and the Sagittarius dwarf), whereas *dark matter only* (DMO) Λ CDM simulations of MW-sized halos (17) produce two to three times this number. Indeed, as shown in Fig. 3, when we consider the DMO counterparts of our LG simulations, the MW and M31 halos each contain an average of 7 – 8 satellites with $V_{\max} > 30$ km/s inside 300 kpc, more than twice the observed number. This is despite the fact that, in order to match the most recent dynamical constraints (13, 14), the average halo masses of M31 and the MW in our simulations are lower than those in which the problem was first identified (3, 18).

The situation changes, however, when we consider the *hydrodynamical* LG simulations. Compared to the DMO case, the halos of dwarf galaxies are less massive, with the loss of baryons and a reduced growth rate leading to a $\sim 15\%$ reduction in V_{\max} . For the abundance of halos below 25 km/s, the reduction in V_{\max} is compounded by the fact that not all low-mass halos host galaxies: at 10 km/s the fraction of luminous systems is well below 10% and decreases even further towards lower masses. Each main galaxy in our simulation has on average only 3 – 4 luminous halos with $V_{\max} > 30$ km/s, in excellent agreement with MW observations (19).

It has also been suggested that constant density cores may be sufficient and indeed necessary to resolve the “too big to fail” problem (20). Observed stellar kinematics of individual dwarf spheroidal galaxies have been interpreted as supporting profiles with profiles (21, 22) while others have argued that they are equally compatible with cusps (23, 24). Whereas N-body simulations clearly predict cusps in CDM halos, it has been shown that supernova feedback may in fact produce cores (25–27), although perhaps not in most dwarf spheroidals (28), via repeated bursts of star formation in the halo center, resulting from an assumed high star formation threshold. By contrast, our star formation and feedback model uses a lower star formation threshold and produces a realistic galaxy population without cores. Hence, whether or not cores

¹Observed stellar mass functions compiled from data by McConnachie (15).

exist, we conclude that they are not necessary to solve the perceived small scale problems of Λ CDM.

Finally, the anisotropy and apparent orbital alignment of the 11 brightest MW satellites, first noticed by Lynden-Bell (29), has been regarded as highly improbable in Λ CDM (5). Fig. 4 compares the observed angular distribution and kinematics to the 11 brightest satellites around one of our resimulated LG galaxies at $z = 0$, as identified in Fig. 1. Both the simulated and observed satellite populations show highly anisotropic distributions.

To characterize the anisotropy, we compute the ratios between the minimal and maximal eigenvalues, c and a , of the reduced inertia tensor (30) defined by the 11 brightest satellites, $I_{\alpha,\beta} = \sum_{i=1}^{11} r_{i,\alpha} r_{i,\beta} / r_i^2$. We find $\sqrt{c/a}$ in the range 0.34 – 0.67 in our simulations, compared to 0.36 for the MW and 0.53 for M31. Clearly, Λ CDM can produce satellite systems with a range of anisotropies, consistent with measurements for both the MW and M31. The origin of the anisotropy may be traced to the effects of the “cosmic web” which impart a degree of coherence to the timing and direction of satellite accretion (31), a scenario consistent with the recently discovered alignment of satellite planes with large scale structures (32).

We conclude that three “problems” often cited as inconsistent with Λ CDM are resolved in simulations that reproduce the dynamical constraints of the Local Group environment coupled to a realistic galaxy formation model. Reionization and feedback allow galaxy formation to proceed only in a tiny subset of dark matter halos, eliminating the “missing satellites” problem. The loss of baryons affects the growth of low-mass halos, leading to a reduction in their maximum circular velocity that solves the “too big to fail” problem. Finally, the structured nature of the Λ CDM “cosmic web” and galaxy formation within it can lead to highly anisotropic satellite distributions with correlated kinematics similar to the “plane of satellites” around the Milky Way.

Our results extend the remarkable success of the Λ CDM model into a new regime. Future observations may yet throw up new challenges but to confront them, the theorist’s armory will need to include a realistic account of galaxy formation.

Acknowledgements We are indebted to Dr. Lydia Heck who looks after the supercomputers at the ICC. This work was supported by the Science and Technology Facilities Council [grant number ST/F001166/1 and RF040218], the European Research Council under the European Unions Seventh Framework Programme (FP7/2007-2013) / ERC Grant agreement 278594 ‘GasAroundGalaxies’, the National Science Foundation under Grant No. PHYS-1066293, the Interuniversity Attraction Poles Programme of the Belgian Science Policy Office [AP P7/08 CHARM]. T. S. acknowledges the Marie-Curie ITN CosmoComp. C. S. F. acknowledges ERC Advanced Grant 267291 ‘COSMIWAY’ and S. W. acknowledges ERC Advanced Grant 246797 ‘GALFORMOD’. This work used the DiRAC Data Centric system at Durham University, operated by the Institute for Computational Cosmology on behalf of the STFC DiRAC HPC Facility (www.dirac.ac.uk), and resources provided by WestGrid (www.westgrid.ca) and Compute Canada / Calcul Canada (www.computeCanada.ca). The DiRAC system is funded by BIS National E-infrastructure capital grant ST/K00042X/1, STFC capital grant ST/H008519/1, STFC DiRAC Operations grant ST/K003267/1, and Durham University. DiRAC is part of the National E-Infrastructure.

References and Notes

1. A. Klypin, A. V. Kravtsov, O. Valenzuela, F. Prada, *Astrophys. J.* **522**, 82 (1999).
2. B. Moore, *et al.*, *Astrophys. J. Let.* **524**, L19 (1999).
3. M. Boylan-Kolchin, J. S. Bullock, M. Kaplinghat, *Mon. Not. R. Astron. Soc.* **415**, L40 (2011).
4. I. Ferrero, M. G. Abadi, J. F. Navarro, L. V. Sales, S. Gurovich, *Mon. Not. R. Astron. Soc.* **425**, 2817 (2012).
5. M. S. Pawlowski, P. Kroupa, *Mon. Not. R. Astron. Soc.* **435**, 2116 (2013).
6. M. R. Lovell, *et al.*, *Mon. Not. R. Astron. Soc.* **420**, 2318 (2012).
7. M. Rocha, *et al.*, *Mon. Not. R. Astron. Soc.* **430**, 81 (2013).
8. S. Garrison-Kimmel, M. Boylan-Kolchin, J. S. Bullock, E. N. Kirby, *Mon. Not. R. Astron. Soc.* **444**, 222 (2014).
9. A. Benítez-Llambay, *et al.*, *ArXiv e-prints* (2014).
10. S. E. Nuza, *et al.*, *Mon. Not. R. Astron. Soc.* **441**, 2593 (2014).
11. M. Vogelsberger, *et al.*, *Nature* **509**, 177 (2014).
12. J. e. a. Schaye, *ArXiv e-prints* (2014).
13. R. E. Gonzalez, A. V. Kravtsov, N. Y. Gnedin, *ArXiv e-prints* (2013).
14. J. Peñarrubia, Y.-Z. Ma, M. G. Walker, A. McConnachie, *Mon. Not. R. Astron. Soc.* **443**, 2204 (2014).
15. A. W. McConnachie, *Astron. J.* **144**, 4 (2012).
16. T. Sawala, *et al.*, *ArXiv e-prints* (2014).
17. V. Springel, *et al.*, *Mon. Not. R. Astron. Soc.* **391**, 1685 (2008).
18. J. Wang, C. S. Frenk, J. F. Navarro, L. Gao, T. Sawala, *Mon. Not. R. Astron. Soc.* **424**, 2715 (2012).
19. J. Peñarrubia, A. W. McConnachie, J. F. Navarro, *Astrophys. J.* **672**, 904 (2008).
20. A. M. Brooks, M. Kuhlen, A. Zolotov, D. Hooper, *Astrophys. J.* **765**, 22 (2013).
21. M. G. Walker, J. Peñarrubia, *Astrophys. J.* **742**, 20 (2011).
22. N. C. Amorisco, N. W. Evans, *Mon. Not. R. Astron. Soc.* **419**, 184 (2012).
23. J. R. Jardel, K. Gebhardt, *Astrophys. J. Let.* **775**, L30 (2013).

24. L. E. Strigari, C. S. Frenk, S. D. M. White, *ArXiv e-prints* (2014).
25. J. F. Navarro, V. R. Eke, C. S. Frenk, *Mon. Not. R. Astron. Soc.* **283**, L72 (1996).
26. F. Governato, *et al.*, *Nature* **463**, 203 (2010).
27. A. Pontzen, F. Governato, *Nature* **506**, 171 (2014).
28. J. Peñarrubia, A. Pontzen, M. G. Walker, S. E. Koposov, *Astrophys. J. Let.* **759**, L42 (2012).
29. D. Lynden-Bell, *Mon. Not. R. Astron. Soc.* **174**, 695 (1976).
30. J. Bailin, M. Steinmetz, *Astrophys. J.* **627**, 647 (2005).
31. N. I. Libeskind, *et al.*, *Mon. Not. R. Astron. Soc.* **363**, 146 (2005).
32. N. G. Ibata, R. A. Ibata, B. Famaey, G. F. Lewis, *Nature* **511**, 563 (2014).
33. V. Springel, *Mon. Not. R. Astron. Soc.* **364**, 1105 (2005).
34. P. F. Hopkins, *Mon. Not. R. Astron. Soc.* **428**, 2840 (2013).
35. J. Schaye, *et al.*, *Mon. Not. R. Astron. Soc.* **402**, 1536 (2010).
36. R. A. Crain, *et al.*, *Mon. Not. R. Astron. Soc.* **399**, 1773 (2009).
37. Y. M. Rosas-Guevara, *et al.*, *ArXiv 1312.0598* (2013).
38. R. P. C. Wiersma, J. Schaye, B. D. Smith, *Mon. Not. R. Astron. Soc.* **393**, 99 (2009).
39. F. Haardt, P. Madau, *Clusters of Galaxies and the High Redshift Universe Observed in X-rays*, D. M. Neumann & J. T. V. Tran, ed. (2001).
40. Planck Collaboration, *et al.*, *ArXiv 1303.5076* (2013).
41. R. P. C. Wiersma, J. Schaye, T. Theuns, C. Dalla Vecchia, L. Tornatore, *Mon. Not. R. Astron. Soc.* **399**, 574 (2009).
42. J. Schaye, T. Theuns, M. Rauch, G. Efstathiou, W. L. W. Sargent, *Mon. Not. R. Astron. Soc.* **318**, 817 (2000).
43. J. Schaye, C. Dalla Vecchia, *Mon. Not. R. Astron. Soc.* **383**, 1210 (2008).
44. J. Schaye, *Astrophys. J.* **609**, 667 (2004).
45. C. Dalla Vecchia, J. Schaye, *Mon. Not. R. Astron. Soc.* **426**, 140 (2012).
46. E. e. a. Komatsu, *Astrophys. J. Suppl.* **192**, 18 (2011).
47. C. Flynn, J. Holmberg, L. Portinari, B. Fuchs, H. Jahreiß, *Mon. Not. R. Astron. Soc.* **372**, 1149 (2006).

- 48. A. Tamm, E. Tempel, P. Tenjes, O. Tihhonova, T. Tuvikene, *Astron. & Astrophys.* **546**, A4 (2012).
- 49. P. S. Behroozi, R. H. Wechsler, C. Conroy, *Astrophys. J.* **770**, 57 (2013).
- 50. A. Jenkins, *Mon. Not. R. Astron. Soc.* **403**, 1859 (2010).
- 51. A. Jenkins, *Mon. Not. R. Astron. Soc.* **434**, 2094 (2013).

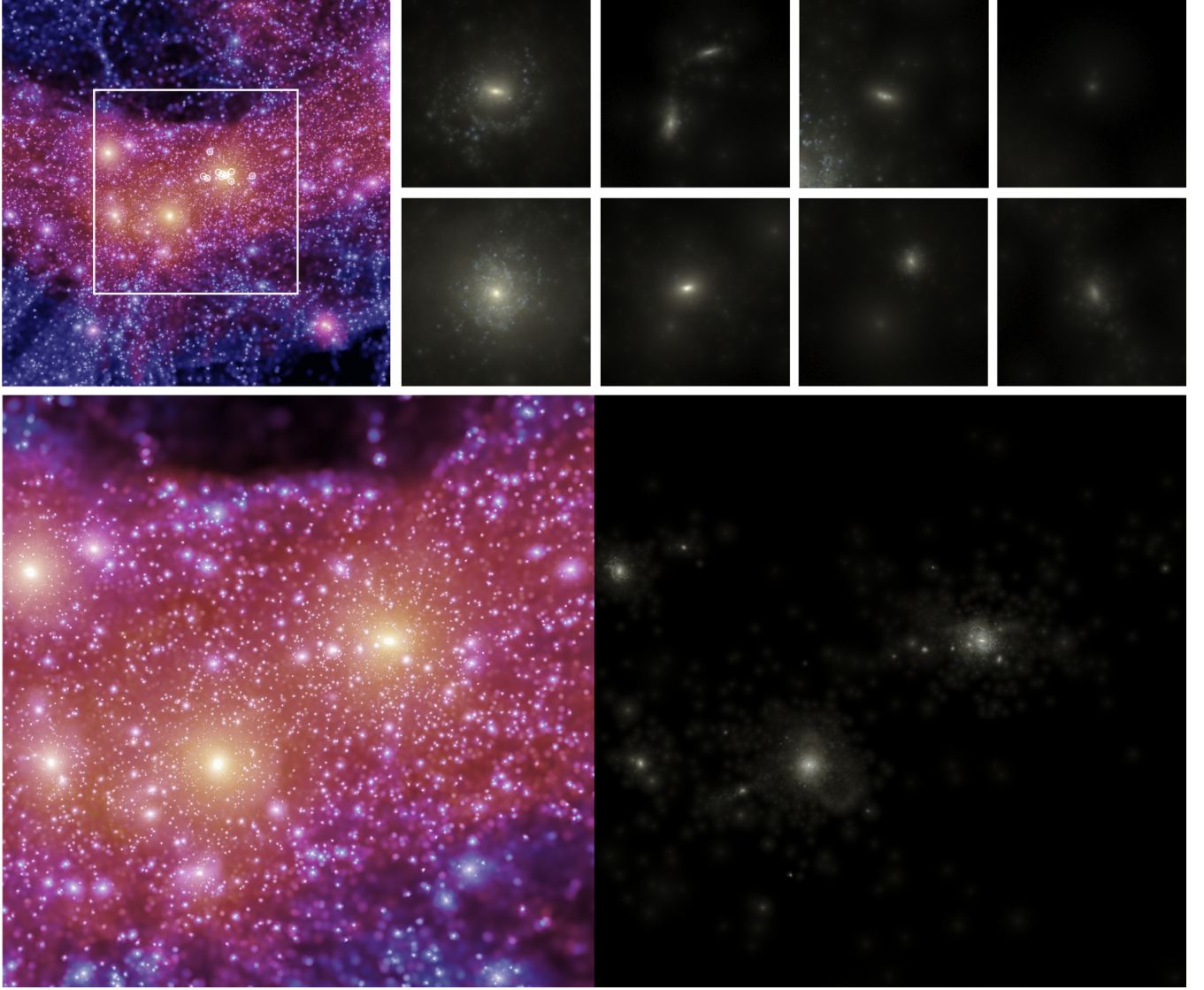


Figure 1: Distribution of dark matter and stars in a Local Group simulation. The top left panel shows the projected dark matter density distribution in one of our resimulations at resolution level L2 in a cube of 4 Mpc on a side. Circles indicate the locations of the eleven brightest satellites of one of the main galaxies, whose spatial distribution is as anisotropic as that of the eleven brightest Milky Way satellites, and which are aligned with the filament that contains most of the halos and galaxies in the region. The main panels contrast the vast number of dark matter substructures (left) with the stellar light distribution (right) in a cube of 2 Mpc, as indicated by the white square in the top left panel. The small panels in the top row are of side length 125 kpc and reveal in more detail the stellar component of some of the different types of galaxies formed in this simulation; central galaxies (first and second column) and satellite galaxies (third and fourth column).

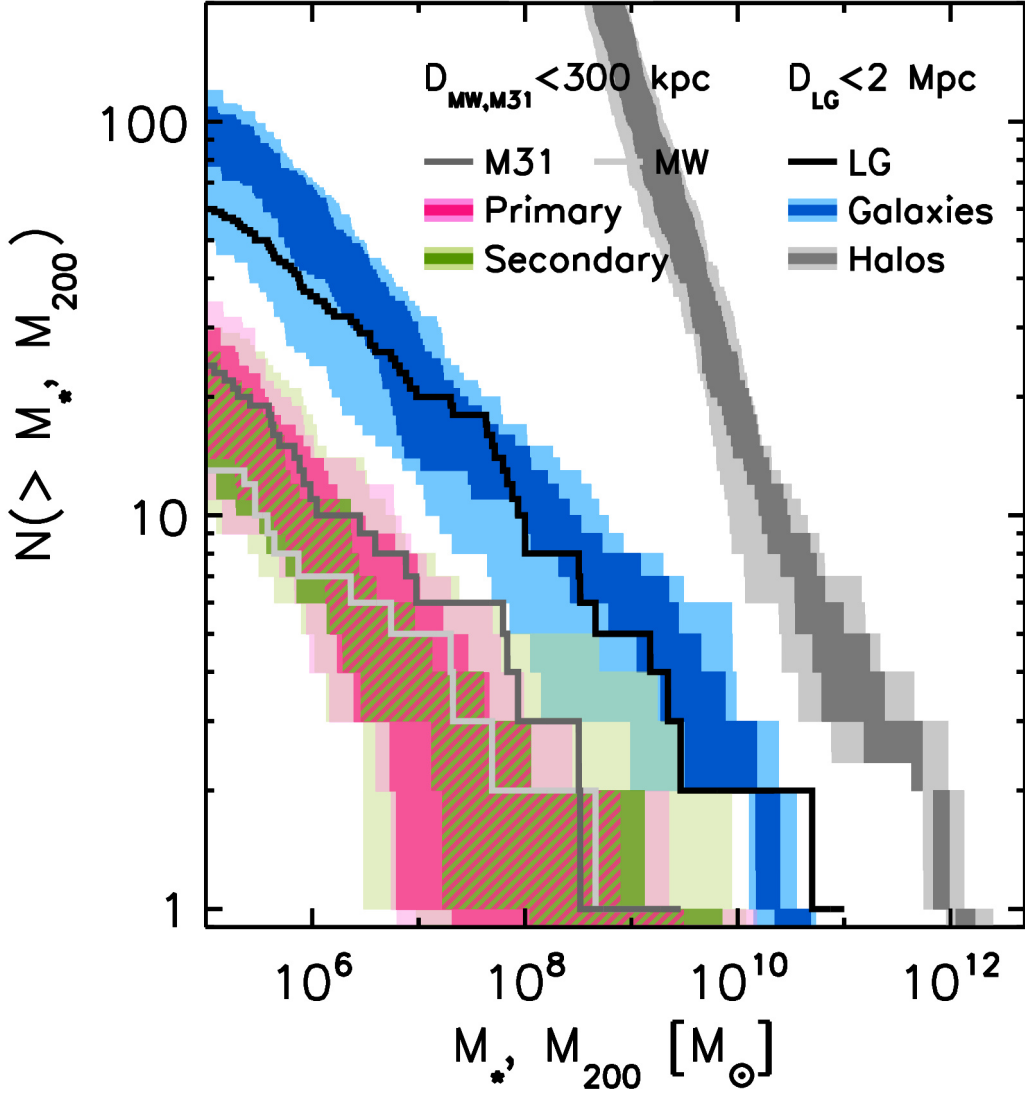


Figure 2: Stellar and halo mass functions in the LG simulations. Red and green bands show the stellar mass functions of satellites within 300 kpc of each of the two main Local Group galaxies, while blue lines show the number of galaxies within 2 Mpc of the Local Group barycenter. The dark color-shaded areas bound the 16th and 84th percentiles; light shaded areas indicate the full range among our twelve Local Group realizations at resolution level L2. For comparison, the grey area corresponds to the mass function of all dark matter halos within 2 Mpc. Solid lines show the measured stellar mass function of the satellites of the Milky Way (light grey) and M31 (dark grey), and of every known galaxy within 2 Mpc from the Local Group barycenter (black, (15)). Note that while the M31 satellite count is likely to be complete to $10^5 M_\odot$, the count of satellites of the MW and the total count within 2 Mpc should be considered as lower limits to the true numbers due to the limited sky coverage and the low surface brightness of dwarf galaxies.

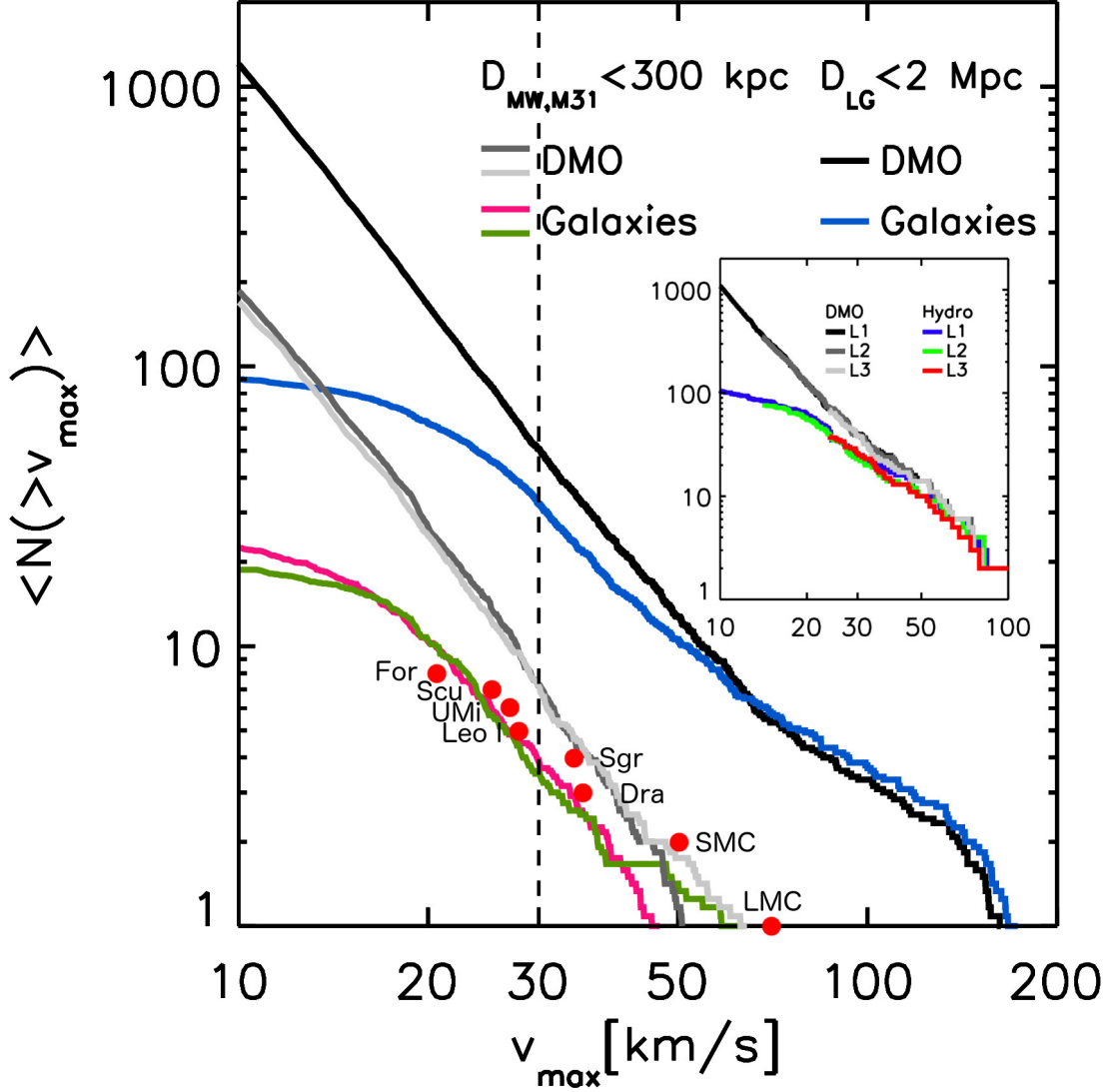


Figure 3: Circular velocity functions of satellites and of all galaxies in the LG environment. Curves show the cumulative number of subhalos as a function of maximum circular velocity, v_{\max} , averaged over 12 LG volumes at resolution level L2. The bottom four curves correspond to subhalos within 300 kpc of each of the two main galaxies; the top two curves to all systems within 2 Mpc from the LG barycenter. Grey/black curves are from dark matter only (DMO) simulations. Colored curves are for systems that contain luminous galaxies in the hydrodynamical runs. The red circles show measurements of the most massive MW satellites by Penarrubia et al. (2008). For guidance, the dashed line denotes a v_{\max} of 30 km s^{-1} . The abundance of satellites with $v_{\max} > 30 \text{ km s}^{-1}$ is halved in the hydrodynamic simulations, and matches the MW observations. At lower values of v_{\max} , the drop in the abundance relative to the DMO case increases as fewer subhalos host an observable galaxy. The inset shows the 2 Mpc curves but for three different resolution runs of the same volume.

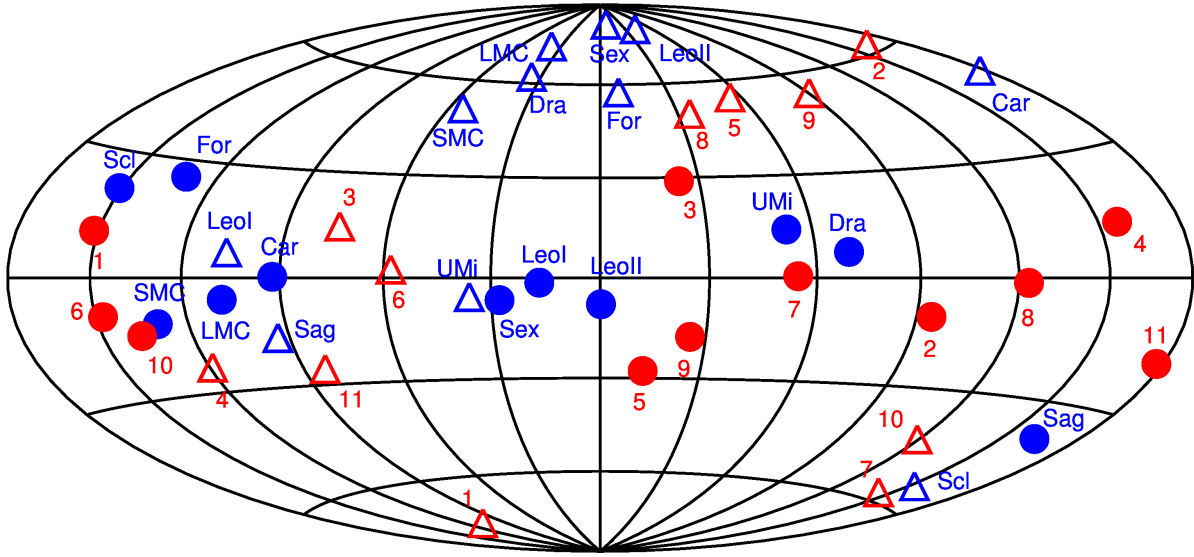


Figure 4: Selecting the brightest satellites, systems as anisotropic as the MW's can be formed in Λ CDM. Red circles show the angular distribution of the eleven brightest satellites of a Milky-Way like system in one of our simulations, while blue circles denote the eleven brightest satellites of the Milky Way. Triangles of the same colors indicate the orientation of the corresponding angular momentum vector. The eleven brightest satellites in the simulated system are distributed on a plane just as flat as those of the Milky Way and several of them have a coherent rotation.

Supplementary Information

Simulation Code

The simulations presented in this paper were performed using the code developed for the *Evolution and Assembly of GaLaxies and their Environments* project (EAGLE (12)). The EAGLE code is a substantially modified version of P-GADGET-3, which itself is an improved version of the publicly available GADGET-2 code (33). Gravitational accelerations are computed using a Tree-PM scheme, while hydrodynamic forces are computed using smoothed particle hydrodynamics (SPH) in the pressure-entropy formalism introduced by Hopkins (34).

EAGLE is an evolution of the models used in the OWLS (35) and GIMIC (36) projects and has been calibrated to reproduce the $z = 0$ stellar mass function accurately from $10^8 M_\odot$ to $10^{11} M_\odot$ in a cosmological volume of 100^3 Mpc^3 . In addition, the EAGLE code also successfully reproduces many other properties and scaling laws of observed galaxy populations, including the evolution of the stellar mass function, and the luminosities, colors and morphologies of galaxies on many different scales.

The subgrid physics model of EAGLE is described in detail by Schaye *et al.* (12). It includes radiative cooling, star formation, stellar evolution and stellar mass loss, and thermal feedback that captures the collective effects of stellar winds, radiation pressure and supernova explosions. It also includes black hole growth fueled by gas accretion and mergers, and feedback from AGN (37).

Following Wiersma *et al.* (38), net cooling rates are computed separately for 11 elements, assuming ionization equilibrium in the presence of uniform UV and X-ray backgrounds from quasars and galaxies (39), and the cosmic microwave background (CMB) (40). Hydrogen is assumed to reionize instantaneously at $z = 11.5$, which is implemented by turning on the ionizing background. At higher redshifts the background is truncated at 1 Ryd, limiting its effect to preventing the formation of molecular hydrogen. During reionization an extra 2 eV per proton mass are injected to account for the increase in the photoheating rates of optically thick gas over the optically thin rates that are used otherwise. For hydrogen this is done at $z = 11.5$, ensuring that the gas is quickly heated to 10^4 K , but for HeII the extra heat is distributed in time following a Gaussian centered at $z = 3.5$ with $\sigma(z) = 0.5$, which reproduces the observed thermal history (41, 42).

The star formation rate is assumed to be pressure-dependent (43) and follows the observed Kennicutt-Schmidt star formation law with a metallicity-dependent density threshold (44). Energy feedback from star formation is implemented using the stochastic, thermal prescription of Dalla Vecchia & Schaye (45). The expectation value for the energy injected per unit stellar mass formed decreases with the metallicity of the gas and increases with the gas density to account for unresolved radiative losses and to help prevent spurious, numerical losses. The injected energy is calibrated to reproduce the observed, $z = 0$ galaxy stellar mass function. On average it is close to the energy available from core collapse supernovae alone (12). Galactic winds develop naturally, without imposing mass loading factors, velocities or directions.

The three different resolution levels of our LG simulations labelled “L1”, “L2” and “L3” have primordial gas (DM) particle masses of $1.0(5.0) \times 10^4 M_\odot$, $1.3(5.9) \times 10^5 M_\odot$ and $1.5(7.3) \times 10^6 M_\odot$, respectively, and maximum gravitational softening lengths of 94 pc, 216 pc and 500 pc. L3 is close to the resolution of the EAGLE L100N1504 simulation. While the resolution

in our highest resolution simulations is comparable to the best simulations of individual MW sized galaxies, it should be noted that with a gravitational softening length of 94 pc, they barely resolve the scale height of the MW thin disk. We cannot truly resolve individual star forming regions, and rely instead on a well-calibrated subgrid physics model to parametrize the star formation and feedback processes. While there is clearly scope for future improvements, the stellar mass function and the circular velocity function of substructures in our simulations are well converged at L2. This indicates that our numerical resolution is sufficient to capture the physical mechanisms of structure formation, gas accretion and outflows, and that the assumptions made in the EAGLE subgrid model do not alter the results significantly.

The high resolution regions always enclose a sphere of at least 2.5 Mpc radius from the LG barycenter at $z = 0$. Outside the high resolution regions, dark matter particles of increasing mass are used to sample the large scale environment of the 100^3 Mpc^3 parent simulation. To investigate the impact of baryons, we also repeated all our simulations as dark matter only (DMO), where the dark matter particle masses in the high resolution region are larger by a factor of $(\Omega_b + \Omega_{DM})/\Omega_{DM}$ than in the corresponding hydrodynamic simulations.

For our study, we have used the same parameter values that were used in the 100^3 Mpc^3 L100N1504 EAGLE simulation (12) independently of resolution. We have found very good convergence in all the relevant properties of our simulated galaxies. While the *Eagle* simulations use the Planck-1 cosmology (40), the Local Group simulations were performed using the WMAP-7 cosmology (46), with density parameters at $z = 0$ for matter, baryons and dark energy of $\Omega_M = 0.272$, $\Omega_b = 0.0455$ and $\Omega_\lambda = 0.728$, respectively, a Hubble parameter of $H_0 = 70.4 \text{ kms}^{-1} \text{ Mpc}^{-1}$, a power spectrum of (linear) amplitude on the scale of $8h^{-1} \text{ Mpc}$ of $\sigma_8 = 0.81$ and a power-law spectral index $n_s = 0.967$.

The Local Group Simulations

Our twelve Local Group regions are zoom simulations based on a DMO simulation (called “DOVE”) of 100^3 Mpc^3 with 1620^3 particles in the WMAP-7 cosmology. The resimulation volumes were selected to match the dynamical constraints of the Local Group. Each volume contains a pair of halos in the mass range $5 \times 10^{11} \text{ M}_\odot$ to $2.5 \times 10^{12} \text{ M}_\odot$, with median values of $1.4 \times 10^{12} \text{ M}_\odot$ for the primary (more massive) halo and $0.9 \times 10^{12} \text{ M}_\odot$ for the secondary (less massive) halo of each pair. The combined masses of the primary and secondary range from $1.6 \times 10^{12} \text{ M}_\odot$ to $3.6 \times 10^{12} \text{ M}_\odot$ with a median mass of $2.3 \times 10^{12} \text{ M}_\odot$, in good agreement with recent estimates of $2.40^{+1.95}_{-1.05} \times 10^{12} \text{ M}_\odot$ based on dynamical arguments and CDM simulations (13), or $2.3 \pm 0.7 \times 10^{12}$ based on equations of motions that take into account the observed velocities of galaxies in the local volume (14). We further require that the two halos be separated by $800 \pm 200 \text{ kpc}$, approaching with radial velocity of $(0 - 200) \text{ kms}^{-1}$ and with tangential velocity below 100 kms^{-1} ; to have no additional halo larger than the smaller of the pair within 2.5 Mpc from the LG barycenter, and to be in environments with a relatively unperturbed Hubble flow out to 4 Mpc.

Excluding substructures, the stellar masses of the Milky Way and M31 analogues in our simulations lie in the range $1.5 - 5.5 \times 10^{10} \text{ M}_\odot$, comparable to the observational estimates for the Milky Way ($5 \times 10^{10} \text{ M}_\odot$ (47)) but lower than those for M31 (10^{11} M_\odot (48)). It should be noted, however, that the Milky Way and M31 both appear to lie above the average stellar-to-halo mass relation derived from abundance matching (49), which is well reproduced by our model

in a large cosmological volume (12). While the predicted abundance of satellites and dwarf galaxies within the Local Group varies with the total mass density, which is dominated by dark matter, it is largely independent of the stellar mass of the main galaxies. The main galaxies in almost all our simulations are extended disk galaxies, reminiscent of the Milky Way and M31, as can be seen for one example in Fig. 1.

The high resolution initial conditions were created using second-order Lagrangian perturbation theory (50). The cosmological parameters and the linear phases of DOVE, which are taken from the public multi-scale Gaussian white noise field PANPHASIA, are given in Tables 1 and 6 by Jenkins (51), which also describes the method used to make the Local Group zoom initial conditions.